In Vivo Autofluorescence Imaging of the Human and Macaque Retinal Pigment Epithelial Cell Mosaic

Jessica I. W. Morgan, **Alfredo Dubra**, **Robert Wolfe**, **William H. Merigan**, and **David R. Williams**
University of Rochester, Center for Visual Science, Rochester, New York

Abstract

Purpose—Retinal pigment epithelial (RPE) cells are critical for the health of the retina, especially the photoreceptors. A recent study demonstrated that individual RPE cells could be imaged in macaque in vivo by detecting autofluorescence with an adaptive optics scanning laser ophthalmoscope (AOSLO). The current study extended this method to image RPE cells in fixating humans in vivo and to quantify the RPE mosaic characteristics in the central retina of normal humans and macaques.

Methods—The retina was imaged simultaneously with two light channels in a fluorescence AOSLO; one channel was used for reflectance imaging of the cones while the other detected RPE autofluorescence. The excitation light was 568 nm, and emission was detected over a 40-nm range centered at 624 nm. Reflectance frames were registered to determine interframe eye motion, the motion was corrected in the simultaneously recorded autofluorescence frames, and the autofluorescence frames were averaged to give the final RPE mosaic image.

Results—In vivo imaging demonstrated that with increasing eccentricity, RPE cell density, and mosaic regularity decreased, whereas RPE cell size and spacing increased. Repeat measurements of the same retinal location 42 days apart showed the same RPE cells and distribution.

Conclusions—The RPE cell mosaic has been resolved for the first time in alert fixating human subjects in vivo using AOSLO. Mosaic analysis provides a quantitative database for studying normal and diseased RPE in vivo. This technique will allow longitudinal studies to track disease progression and assess treatment efficacy in patients and animal models of retinal disease.

The retinal pigment epithelium (RPE) is a monolayer of cells directly behind the photoreceptors that has several functions including participation in the regeneration of retina in the visual cycle and the phagocytosis of photoreceptor outer segments.[1] Healthy RPE cells are critical for maintaining the normal structure of the retina and for preserving normal photoreceptor function. Indeed, abnormal RPE cells contribute to disease mechanism and progression in numerous retinal diseases, including age-related macular degeneration, Stargardt's dystrophy, Best's disease, and others.[1]

Despite the important role of the RPE in retinal health, little is known about the RPE cell mosaic structure, mainly because histologic studies on cell density and packing disagree.[2–7] In addition, drug and molecular treatments for retinal diseases are advancing[8] such that in vivo metrics must be developed to assess disease progression and treatment efficacy on a cellular

Corresponding author: Jessica I. W. Morgan, Meliora 274, University of Rochester, Rochester, NY 14627; jwmorgan@mail.med.upenn.edu.

scale. The present study addresses these points by providing in vivo images of the normal human RPE cells and by quantifying the spatial arrangement of the RPE mosaic.

There has been considerable effort recently to develop in vivo retinal imaging modalities with cellular resolution. The use of adaptive optics (AO), which involves measuring the higher-order optical aberrations in the eye with a wavefront sensor and correcting these aberrations with a wavefront corrector, has allowed improvements in contrast and resolution such that it has become possible to routinely characterize the photoreceptor mosaic in both normal and diseased eyes in vivo.[9–16] In addition, the combination of AO with a scanning laser ophthalmoscope (SLO) has allowed for the visualization of individual RPE cells in reflectance imaging in retinal locations where the photoreceptor mosaic is missing in cone–rod dystrophy.[17]

In vivo reflectance imaging of the RPE cells in normal retina has not been possible with AOSLO techniques, because the axial resolution in combination with the unique waveguiding nature of the overlying photoreceptors obscures signal from the RPE. However, the RPE cells are unique in that they accumulate lipofuscin granules in their cytoplasm through the processes of the visual cycle and phagocytosis.[18,19] Lipofuscin naturally consists of several autofluorescence molecules,[20–22] and therefore the lipofuscin granules provide an autofluorescence signal, unique to the RPE layer, that allows the RPE layer to be imaged.[23]

In vivo studies of retinal autofluorescence[23–31] have shown that the excitation and the emission spectra of lipofuscin are broad,[25] that the RPE autofluorescence signal varies over retinal eccentricity,[28] and that the signal increases as a function of age until the eighth decade of life, after which the signal tends to decrease.[28,32] The lipofuscin autofluorescence signal has been used to image macroscopic features of the RPE layer in both normal and diseased retinas.[23,26,27,29–31]

This study presents the first in vivo images of the complete RPE cell mosaic in normal human retinas by using a combination of lipofuscin autofluorescence, AOSLO, and simultaneous dual-wavelength imaging and registration. We have previously demonstrated RPE cell imaging capabilities in the primate retina.[33] In the present study, we validated the technique by comparing in vivo images of the macaque RPE mosaic to ex vivo images at the same retinal location. In addition, the spatial arrangement of the RPE mosaic was quantified in normal human and macaque retinas. The ability to image the complete RPE cell mosaic noninvasively in vivo allows morphologic studies of normal and diseased RPE cells and will provide a method of tracking disease progression and treatment efficacy in patients and animal models of disease.

Methods

Human Subjects and Animals

In human volunteer subjects, written informed consent was obtained after the nature and possible consequences of the study were explained. Three human volunteers were used in this study: two male subjects ages 25 and 30 and one female subject age 26. The subjects were given a complete ophthalmic examination including fundus photography. The data presented in this study were collected over two to four imaging sessions for each subject, with each session lasting approximately 2 hours. At the beginning of each AO imaging session, the eyes were dilated and cycloplegia induced with one drop each of phenylephrine hydrochloride (2.5%) and tropicamide (1%). The subject's head was aligned and stabilized with the use of a dental impression on a bite bar. The subjects were asked to fixate as best as possible at a distant target to allow imaging of various retinal locations.

Two monkeys were used in the study: Monkey 320 was an 8-year-old male *Macaca fascicularis*, and monkey 903 was an 11-year-old male *Macaca nemestrina*. During the experiments involving nonhuman primates, the macaques were anesthetized with isoflurane (1.0%–3.0%), body temperature was monitored, and pupils were dilated and cycloplegia induced with one drop each of phenylephrine hydrochloride (2.5%) and tropicamide (1%). A lid speculum held the eye open for imaging, and a rigid gas-permeable contact lens was used to protect the cornea.[34] The animal's head and pupil of the eye were aligned with the imaging system by a headpost rotation mount and a three-axis translation stage.

Axial lengths were used to determine the scale of the retinal images by linearly scaling the LeGrand model eye.[35] This method of linear scaling was found to have good agreement with the scale as determine by ex vivo imaging. In the macaques, axial length was measured by averaging 10 measurements made by B-scan ultrasound. Human subjects' axial lengths were measured with an ocular biometer (IOLMaster; Carl Zeiss Meditec, Jena, Germany).

All research presented in this study was approved by the institutional review boards for human studies and animal research at the University of Rochester. All the experiments in human volunteers adhered to the tenets of the Declaration of Helsinki and were HIPAA-compliant. The experiments involving macaques complied with the ARVO Statement for the Use of Animals in Ophthalmic and Vision Research. All imaging light exposures adhered to the MPE limits set by the ANSI standard.[36]

Autofluorescence Imaging

The fluorescence AOSLO used in this experiment is described elsewhere.[33] Three lasers were simultaneously scanned on the retina: an 830 nm laser diode (LD) or a 794-nm superluminescent diode (SLD) was used for reflectance imaging, a 904-nm LD was used for wavefront sensing, and an Ar/Kr tunable laser was used for autofluorescence excitation. The two imaging detectors were an avalanche photodiode (APD; C309025-DTC; Perkin-Elmer, Wellesley, MA) for reflectance imaging and a photomultiplier tube (PMT; H7422-40; Hamamatsu. Hamamatsu City, Japan) with a transimpedance amplifier (HCA-10M-100K; Femto Messtechnik GmbH, Berlin, Germany) for autofluorescence imaging.

Lipofuscin autofluorescence was excited with 568-nm light from the Ar/Kr laser, and fluorescence emission was collected over a 40-nm bandwidth centered at 624 nm. To overcome the problem of weak autofluorescence signal, two spectral bands were used to record two simultaneous videos: A high signal-to-noise ratio video of the photoreceptors using reflectance imaging in the near infrared and a low signal autofluorescence video of the RPE using 568-nm light for excitation. Both the high signal reflectance movies of the photoreceptors and the low signal autofluorescence movies of the RPE cells exhibited the same retinal motion because they were recorded simultaneously. To correct for motion of the eye, we registered the sequence of reflectance images by using the normalized cross-correlation algorithm defined as

$$C_{r,f}(m,n) = \frac{\sum_{i,j} r(i,j) f(m+i, n+j)}{\sqrt{\sum_{i,j} r(i,j)^2 \sum_{p,q} f(p,q)^2}}$$

where r and f denote the images that are being compared, indices represent the image pixels along the vertical and horizontal directions, and the sums are performed only over the areas of image overlap. The images were then shifted and averaged together. The movement correction associated with each reflectance frame was then applied to the corresponding autofluorescence frame, and the autofluorescence frames were averaged to produce the final image. The final

autofluorescence images shown in this study are the registered sum of 1000 to 1700 individual frames.

Ex Vivo Methods

After imaging, one macaque was euthanatized for histologic analysis of the cell mosaics. The monkey was perfused with saline followed by 4% paraformaldehyde. After additional fixation in the eye cup, the retinas were removed, wholemounted on a slide in mounting medium (Vectashield; Vector Laboratories, Burlingame, CA), and covered with a coverslip. The RPE and choroid were left attached to the photoreceptors and inner retinal layers. The ex vivo tissue was then imaged with a confocal fluorescence microscope (Laser Scanning Microscope, LSM510Meta; Carl Zeiss Meditec) to view the cone and RPE cell mosaics with 543-nm light for autofluorescence excitation in combination with a long-pass 560-nm emission filter.

Image Analysis

For each RPE image, geometrical characteristics of the RPE cell mosaic were studied. RPE cells were identified manually by using ImageJ (National Institutes of Health, Bethesda, MD; developed by Wayne Rasband, National Institutes of Health, Bethesda, MD; available at http://rsb.info.nih.gov/ij/index.html), and their x, y coordinates were stored. Cell density was determined by dividing the total number of cells counted by the retinal area sampled. A 6% uncertainty in RPE cell density was assumed based on the results of Li and Roorda[37] for manual cell selections. To examine RPE cell regularity, a Voronoi domain analysis[38,39] was performed by determining all pixels in the image that were closer to one cell's center than to any other cell's center. The Voronoi cell boundaries were determined by finding the midpoints and vertices between neighboring cell x, y coordinates, and from those boundaries, the number of Voronoi neighbors and the size of each Voronoi cell was calculated. The nearest neighbor distance (NND) for each cell was also determined by taking the minimum of the distances from that cell center to every other cell center in the mosaic. NND was compared with the expected spacing of cell centers in a triangularly packed mosaic with the same cell density. The expected triangular spacing is given by the equation:

$$s=\left(\frac{2}{\sqrt{3}D}\right)^{1/2},$$

where s is the spacing between the centers of triangularly packed cells and D is the cell density, as described by Coletta and Williams.[40] All measurement uncertainties are expressed according to the NIST technical note 1297.[41] For the large RPE mosaic in Figure 1, the image was divided into subregions and analyzed as a function of eccentricity from the fovea. The foveal center was taken as the center of the avascular zone. Square areas, 1° in visual angle per side, of the mosaic were analyzed from the fovea along the vertical and horizontal meridians, and in the nasal-superior, nasal-inferior, temporal-superior, and temporal-inferior directions.

Cone photoreceptor imaging was also performed, and the statistics of the cone photoreceptor mosaic were compared to that of the RPE cells. For the in vivo cone counting, a computerized automated selection program (in MatLab; The Math Works, Natick, MA)[37] was used to estimate the (x, y) cone locations. A 6% uncertainty was also assumed for cone density.[37] For the ex vivo confocal microscope images of the cone photoreceptors, the x, y coordinate locations were determined manually using ImageJ. Cone density, Voronoi area, number of Voronoi neighbors, and NND were then determined for the cone photoreceptor mosaic using the same method as for the RPE analysis.

Results

The In Vivo RPE Mosaic

Figure 1 shows the mosaic of the RPE cells from the right eye of a macaque, obtained in vivo using the AOSLO autofluorescence imaging technique. Each RPE cell nucleus was a dark circle, surrounded by a ring of autofluorescence from the lipofuscin located in the cytoplasm of the RPE cell. Every RPE cell in the central fovea and surrounding regions was resolved in this image. The avascular region of this eye was also observed. Retinal blood vessels appeared as shadows overlying the RPE mosaic. Blood vessels appeared in the image at locations eccentric to the fovea.

Statistics of the RPE cell mosaic were determined from Figure 1, as described in the image analysis section, and the results are displayed in Table 1. Figure 2 shows the RPE cell density as a function of eccentricity as determined from the analysis of Figure 1.

Figure 3 shows the Voronoi domain analysis for the RPE mosaic shown in Figure 1. Each Voronoi cell is composed of the area of the image that is closer to a given RPE cell center than any other RPE cell center. From the Voronoi domain analysis, the number of neighboring Voronoi cells is determined. In Figure 3, a green Voronoi cell has exactly six neighbors. For all locations except 4° N, 3° T, 3° I, and 3° T–3° I, at least 60% of the Voronoi cells had six neighboring cells. Table 1 shows the mean number of Voronoi neighbors and the standard deviation of the number of neighbors for each location analyzed. The SD of the number of neighboring cells provides a metric for the packing arrangement. In general, the standard deviations of number of neighbors increase with increasing eccentricity, corresponding to a decrease in the regularity of the packing arrangement. Table 1 also shows that the mean and standard deviation of the Voronoi domain area increases with eccentricity (Fig. 3). Increased deviation of Voronoi area also corresponds with decreased regularity of the mosaic.

It was also observed that the SD of the observed NND increased with the mean NND, which once again corresponds to a decrease in mosaic regularity. Using the equation from Coletta and Williams,[40] the expected NND for a triangularly packed RPE cell mosaic of equivalent cell density for a given location is calculated in Table 1. The ratio of observed NND to the expected NND is also provided. A lower ratio corresponds to a less regular cell mosaic. The departure of NND from that of a regular triangular mosaic is more than that expected by positional noise from selection of the cell centers alone.

Figure 4 depicts two in vivo images of the RPE mosaic from the left eye of a second macaque, monkey 903. The corresponding statistics are shown in Table 2. As in the previous case, RPE cell density and mosaic regularity decreased as eccentricity increased. As well, RPE cell spacing and Voronoi area increased with increasing eccentricity. For the 2° nasal image, 59.9% of the Voronoi domain cells have six neighboring cells. In comparison, for the image located at approximately 6.5° temporal, 1° inferior, only 46.0% of the cells have six neighbors. Thus, the RPE mosaic is more triangularly packed at the lower eccentricity.

In vivo images of the human RPE mosaic at three different eccentricities are shown in Figure 5 for human subject 3. Again, each RPE cell is observed as a dark nucleus and an autofluorescence ring from the lipofuscin in the cell's cytoplasm. Table 2 presents the statistical results of the spatial arrangement of the in vivo images of the RPE cell mosaics from human subjects. Figure 6 illustrates the RPE cell density for three normal human subjects as a function of eccentricity. In general, mean RPE cell density decreased as eccentricity from fixation increased. However, for individual subjects, RPE cell density did not decrease monotonically; subjects had local maxima in RPE cell density at eccentricities other than the fovea. In addition, RPE cell density varied between subjects.

Imaging the RPE Mosaic Over Time

Figure 7 shows two in vivo images of the RPE mosaic in the right eye of human subject 1 at 15° superior to fixation. The two images were taken 42 days apart and have a normalized cross-correlation coefficient of 0.95. Each RPE cell in the first image is in the same location in the second image. The comparison demonstrates the ability to repetitively image the same retinal location in vivo across time, which can be very useful in tracking changes in the RPE mosaic in normal aging, in retinal disease, and in response to therapy for retinal disease.

Comparison of the RPE Mosaic and the Cone Photoreceptor Mosaic

The AOSLO autofluorescence imaging technique with simultaneous reflectance imaging and registration yields images of the cone photoreceptor mosaic at the same locations as the RPE cells. Figure 8 shows the cone mosaic and RPE cell mosaic at approximately 4.5° nasal, 4.5° inferior in the left eye of monkey 320. The overlying cone mosaic does not appear to alter the autofluorescence image of the RPE cells. This agrees with the result published by Burns et al. [42] and Prieto et al. [43] that the cones do not waveguide autofluorescent light from the RPE. Apparently, light from RPE autofluorescence passes through the photoreceptors and out of the eye relatively unperturbed by the high refractive index variations associated with the photoreceptor mosaic. Table 3 provides the statistics of the spatial arrangement for the two cell classes at that location. As illustrated in Figure 8c, points of high intensity in the autofluorescence image do not necessarily correspond to overlying cone cell centers. More than 50% of the cells in both the RPE and cone mosaics have exactly six Voronoi neighbors. Both the RPE cell mosaic and the cone photoreceptor mosaic exhibit a disordered, packed spatial arrangement that departs from a triangular lattice, as has been described for the cone mosaic. [44]

Histologic Validation of In Vivo Images

Figure 9 depicts the results of histologic validation of in vivo RPE mosaic imaging. Figure 9a shows the RPE mosaic imaged in vivo at approximately 6° temporal, 4.5° superior in the left eye of monkey 903. Figure 9b shows the RPE mosaic at the same location imaged postmortem with a confocal microscope; the retinal blood vessels are not observed in the postmortem image. Each RPE cell in the in vivo image corresponds to an RPE cell in the ex vivo image. Except for RPE cells underlying retinal blood vessels, every RPE cell imaged postmortem using microscopy can be observed in vivo. The figure also depicts the cone photoreceptor mosaic, as imaged postmortem. Table 3 provides the statistics of the spatial arrangement for the two cell classes.

Discussion

In Vivo Imaging

With the combination of AOSLO, autofluorescence, dual imaging, and registration techniques, the RPE mosaic was resolved noninvasively in vivo. These techniques have allowed the full characterization of the RPE mosaic, in vivo, in a series of locations of the human and macaque retina, including the smaller RPE cells located in the central macula. The technique was validated by using both in vivo and ex vivo imaging methods to observe the RPE cells in the same retinal location in the macaques.

Although the RPE cell layer forms a mostly regular mosaic of triangularly packed cells, the cells are known to show large degrees of heterogeneity, especially in melanin and lipofuscin granule content. [45] The images in the present study (for example, Fig. 8b) show variability between cells in the quantity of autofluorescence, with some cells exhibiting distinct points of autofluorescence. Those "hot spots" of autofluorescence are preferentially located at the RPE

Voronoi cell vertices and do not necessarily correspond to overlying cones. Thus, those bright points are not simply a result of the waveguiding of autofluorescence light back through the cone. That conclusion agrees with a previous report that suggests autofluorescence light is not waveguided through the cones.[42,43] Rather, the "hot spots" are probably caused by individual lipofuscin granules or clumps of granules. Lipofuscin granules are known to localize close to the RPE cell borders when low lipofuscin granule density is present,[46] as would be expected for all the young, normal subjects[19] and animals involved in the present study. Therefore, the AOSLO autofluorescence method allows not only resolution of the RPE mosaic, but allows subcellular features of the RPE cells, such as clumps of lipofuscin granules and the cell nucleus, to be studied in vivo. The ability to image these features may allow future studies regarding the heterogeneous distribution and accumulation of lipofuscin granules to be performed in vivo.

Comparison to Other Studies

It is difficult to compare the human RPE cell densities found in this study with postmortem studies in the literature, mainly because of differences in the examined retinal locations, area and subject age. Panda-Jonas et al.[4] showed density over eccentricity for the four retinal meridians and across age. They found that RPE cell density decreased as a function of eccentricity and that the density does not vary markedly across the different meridians in central and midperipheral retina. Panda-Jonas et al.[4] reported an RPE cell density of 3510 ± 520 cells/mm^2 at 2 to 5 mm superior retina at an average age of 58.6 years. Combining the human measurements in the present study to include all locations at 2 to 5 mm superior ($7°–16°$ superior), the average RPE cell density was 5280 ± 230 RPE cells/mm^2 for three subjects of age 30, 26, and 25 years. Even correcting for the different ages of retina between the two studies, the RPE cell density measured in this study is higher than that of Panda-Jonas et al.[4] Another study by Watzke et al.[3] measured RPE cell density as 4830 ± 760 RPE cells/mm^2 at 4 mm temporal retina. That study agrees with the measured RPE cell density in this study of 4650 ± 640 RPE cells/mm^2 at $15°$ superior retina—approximately 4.3 mm superior. Finally, in a third study, Gao and Hollyfield[2] measured RPE cell density at 13 mm temporal as 5490 ± 320 RPE cells/mm^2. That measurement is higher than the density of 4100 ± 80 RPE cells/mm^2 found at $20°$ superior (approximately 6 mm) in this study. In all, the literature shows large ranges of RPE cell density that have high variability across age, area, location, and retina.[2–7] Within the present study, there was also variability between subjects. Thus, the large variability observed between studies could be caused by a sampling artifact. This emphasizes the value of performing in vivo measurements to assess and track the progression of cell death in patients with retinal disease.

In addition to RPE cell density, the present study examined the regularity of the mosaic by evaluating the number of Voronoi domain neighbors, Voronoi domain area, and NND. We found that mosaic regularity depends on the retinal location; in general, regularity decreased as eccentricity from the fovea increased. In a histologic study, Watzke et al.[3] used a metric of cell shape to compare hexagonality with retinal location and age. They found no regional differences in RPE hexagonality; however, they did find a decrease in hexagonality with age. We did not investigate age differences, as the age range for the three human subjects tested was only 25 to 30 years. Because of the intersubject variability in RPE cell density observed both in this study and in other studies,[2–6] those types of regularity analyses may be necessary for early disease diagnosis. For example, Baraas et al.,[38] using Voronoi domain analysis, found a significant difference in the regularity of a tritan cone mosaic, even though the total cone density was considered normal. Likewise, regularity metrics of the RPE mosaic may prove more useful for early disease diagnosis than simply RPE cell density alone.

Comparing the Cone and RPE Mosaics

In addition to the images of the RPE mosaic, the method described in this study allows images of the cone photoreceptor mosaic to be obtained simultaneously (Fig. 8). According to Snodderly et al.,[47] the cone to RPE ratio is approximately 3.8 cones/RPE cell at 0.9 mm inferior (approximately 4.5° inferior) for the rhesus monkey, whereas the present study found 5.43 cones/RPE cell at a location approximately 4.5° nasal, 4.5° inferior. Differences in the measured cone to RPE cell ratio between our study and Snodderly et al. include differences in primate species and differences in retinal location. Also, they measured RPE density but used average cone density from studies of different animals. The advantage in our study is that the same retinal location in the same animal was observed for both cell layers. The ability to image both the RPE cell and cone mosaics will allow researchers to study the regional effects of disease and follow disease progression in both retinal layers in vivo.

Observations of Retinal Change

The ability to image the RPE mosaic also allows visualization of changes in the RPE mosaic on an individual cellular level. In a separate ongoing experiment,[48] changes in the macaque RPE mosaic were observed as a result of light exposures below the ANSI standard, which is meant to ensure retinal safety. Those changes include a transient decrease in autofluorescence intensity followed by either full recovery or permanent structural damage. After those observations, further imaging of the RPE cell mosaic was not performed in human retinas until thorough light-induced damage and safety studies could be completed in the macaque. No changes in RPE structure have been observed at any time in human retinas. In results to be presented elsewhere, we will show the threshold exposure for those changes and demonstrate safe conditions for RPE mosaic imaging.

Conclusions

This study demonstrates a novel ability to image the complete RPE cell mosaic in vivo in human retina and provides initial quantitative analysis for a normative database of the RPE mosaic characteristics in human and macaque retina. That ability is essential for advancing the study of the morphology of normal and diseased retina to living patients rather than donor retina. Providing a normative database of RPE mosaic statistics will help determine baseline information for future studies of diseased retina. Furthermore, the ability to image the RPE in vivo in normal and diseased retina may lead to early diagnosis of retinal disease. Finally, the ability to image the same retinal location over time will allow disease progression and treatment efficacy studies to be done in vivo on a cellular level in patients and animal models of retinal disease.

Acknowledgments

References

1. Strauss O. The retinal pigment epithelium in visual function. Physiol Rev 2005;85(3):845–881. [PubMed: 15987797]

2. Gao H, Hollyfield JG. Aging of the human retina: Differential loss of neurons and retinal pigment epithelial cells. Invest Ophthalmol Vis Sci 1992;33(1):1–17. [PubMed: 1730530]

3. Watzke RC, Soldevilla JD, Trune DR. Morphometric analysis of human retinal pigment epithelium: correlation with age and location. Curr Eye Res 1993;12(2):133–142. [PubMed: 8449024]

4. Panda-Jonas S, Jonas JB, Jakobczyk-Zmija M. Retinal pigment epithelial cell count, distribution, and correlations in normal human eyes. Am J Ophthalmol 1996;121:181–189. [PubMed: 8623888]

5. Harman AM, Fleming PA, Hoskins RV, Moore SR. Development and aging of cell topography in the human retinal pigment epithelium. Invest Ophthalmol Vis Sci 1997;38(10):2016–2026. [PubMed: 9331265]

6. Del Priore LV, Kuo Y-H, Tazel TH. Age-related changes in human RPE cell density and apoptosis proportion in situ. Invest Ophthalmol Vis Sci 2002;43:3312–3318. [PubMed: 12356840]

7. Leung IY-F, Sandstrom MM, Zucker CL, et al. Nutritional manipulation of primate retinas, II: Effects of age, n-3 fatty acids, lutein, and zeaxanthin on retinal pigment epithelium. Invest Ophthalmol Vis Sci 2004;45(9):3244–3256. [PubMed: 15326147]

8. Maguire AM, Simonelli F, Pierce EA, et al. Safety and Efficacy of gene transfer for Leber's congenital amaurosis. N Engl J Med 2008;358:2240–2248. [PubMed: 18441370]

9. Liang J, Williams DR, Miller DT. Supernormal vision and high-resolution retinal imaging through adaptive optics. J Opt Soc Am A 1997;14(11):2884–2892.

10. Hofer H, Chen L, Yoon GY, et al. Improvement in retinal image quality with dynamic correction of the eye's aberrations. Opt Express 2001;8(11):631–643. [PubMed: 19421252]

11. Roorda A, Williams DR. The arrangement of the three cone classes in the living human eye. Nature (Lond) 1999;397:520–522. [PubMed: 10028967]

12. Roorda A, Romero-Borja F, Donnelly WJ III, et al. Adaptive optics scanning laser ophthalmoscopy. Opt Express 2002;10(9):405–412. [PubMed: 19436374]

13. Hermann B, Fernandez EJ, Unterhuber A, et al. Adaptive-optics ultrahigh-resolution optical coherence tomography. Opt Lett 2004;29(18):2142–2144. [PubMed: 15460883]

14. Carroll J, Neitz M, Hofer H, et al. Functional photoreceptor loss revealed with adaptive optics: an alternate cause for color blindness. Proc Natl Acad Sci U S A 2004;101(22):8461–8466. [PubMed: 15148406]

15. Wolfing JI, Chung M, Carroll J, et al. High-resolution retinal imaging of cone-rod dystrophy. Ophthalmology 2006;113:1014–1019.

16. Choi SS, Doble N, Hardy JL, et al. In vivo imaging of the photoreceptor mosaic in retinal dystrophies and correlations with visual function. Invest Ophthalmol Vis Sci 2006;47:2080–2092. [PubMed: 16639019]

17. Roorda A, Zhang Y, Duncan JL. High-resolution in vivo imaging of the RPE mosaic in eyes with retinal disease. Invest Ophthalmol Vis Sci 2007;48(5):2297–2303. [PubMed: 17460294]

18. Radu RA, Mata NL, Nusinowitz S, et al. Treatment with isotretinoin inhibits lipofuscin accumulation in a mouse model of recessive Stargardt's macular degeneration. Proc Natl Acad Sci U S A 2003;100 (8):4742–4747. [PubMed: 12671074]

19. Feeneyburns L, Hilderbrand ES, Eldridge S. Aging human RPE: morphometric analysis of macular, equatorial, and peripheral cells. Invest Ophthalmol Vis Sci 1984;25(2):195–200. [PubMed: 6698741]

20. Eldred GE, Katz ML. Fluorophores of the human retinal pigment epithelium: separation and spectral characterization. Exp Eye Res 1988;47:71–86. [PubMed: 3409988]

21. Sparrow JR, Fishkin N, Zhou J, et al. A2E, a byproduct of the visual cycle. Vision Res 2003;43:2983–2990. [PubMed: 14611934]

22. Fishkin NE, Sparrow JR, Allikmets R, Nakanishi K. Isolation and characterization of a retinal pigment epithelial cell fluorophore: an all-trans-retinal dimer conjugate. Proc Natl Acad Sci U S A 2005;102 (20):7091–7096. [PubMed: 15870200]

23. von Ruckmann A, Fitzke FW, Bird AC. Distribution of fundus autofluorescence with a scanning laser ophthalmoscope. Br J Ophthalmol 1995;79:407–412. [PubMed: 7612549]

24. Delori FC. Spectrophotometer for noninvasive measurement of intrinsic fluorescence and reflectance of the ocular fundus. Appl Opt 1994;33(31):7439–7452.

25. Delori FC, Dorey CK, Staurenghi G, et al. In vivo fluorescence of the ocular fundus exhibits retinal pigment epithelium lipofuscin characteristics. Invest Ophthalmol Vis Sci 1995;36(3):718–729. [PubMed: 7890502]

26. von Ruckmann A, Fitzke FW, Bird AC. Fundus autofluorescence in age-related macular disease imaged with a laser scanning ophthalmoscope. Invest Ophthalmol Vis Sci 1997;38:478–486. [PubMed: 9040481]

27. Lois N, Halfyard AS, Bird AC, Fitzke FW. Quantitative evaluation of fundus autofluorescence imaged "in vivo" in eyes with retinal disease. Br J Ophthalmol 2000;84:741–745. [PubMed: 10873986]

28. Delori FC, Goger DG, Dorey CK. Age-related accumulation and spatial distribution of lipofuscin in RPE of normal subjects. Invest Ophthalmol Vis Sci 2001;42(8):1855–1866. [PubMed: 11431454]

29. Holz FG, Bellman C, Staudt S, et al. Fundus autofluorescence and development of geographic atrophy in age-related macular degeneration. Invest Ophthalmol Vis Sci 2001;42(5):1051–1056. [PubMed: 11274085]

30. Lois N, Halfyard AS, Bird AC, et al. Fundus autofluorescence in Stargardt macular dystrophy-fundus flavimaculatus. Am J Ophthalmol 2004;138(1):55–63. [PubMed: 15234282]

31. Bindewald A, Jorzik JJ, Loesch A, et al. Visualization of retinal pigment epithelial cells in vivo using digital high-resolution confocal scanning laser ophthalmoscopy. Am J Ophthalmol 2004;137(3):556–558. [PubMed: 15013882]

32. Wing GL, Blanchard GC, Weiter JJ. The topography and age relationship of lipofuscin concentration in the retinal pigment epithelium. Invest Ophthalmol Vis Sci 1978;17(7):601–607. [PubMed: 669891]

33. Gray DC, Merigan W, Wolfing JI, et al. In vivo fluorescence imaging of primate retinal ganglion cells and retinal pigment epithelial cells. Opt Express 2006;14:7144–7158. [PubMed: 19529085]

34. Metha AB, Crane AM, Rylander HGI, et al. Maintaining the cornea and the general physiological environment in visual neurophysiology experiments. J Neurosci Methods 2001;109:153–166. [PubMed: 11513950]

35. Wyszecki, G.; Stiles, WS. Color Science: Concepts and Methods, Quantitative Data and Formulae. Vol. 2. New York: John Wiley & Sons; 1982.

36. ANSI. ANSI publication no. Z136.1–2007. Orlando, FL: Laser Institute of America; 2007. American National Standard for Safe Use of Lasers.

37. Li KY, Roorda A. Automated identification of cone photoreceptors in adaptive optics retinal images. J Opt Soc Am A 2007;24(5):1358–1363.

38. Baraas RC, Carroll J, Gunther KL, et al. Adaptive optics retinal imaging reveals S-cone dystrophy in tritan color-vision deficiency. J Opt Soc America A 2007;24(5):1438–1447.

39. Galli-Resta L, Novelli E, Kryger Z, et al. Modelling the mosaic organization of rod and cone photoreceptors with a minimal-spacing rule. Eur J Neurosci 1999;11:1461–1469. [PubMed: 10103140]

40. Coletta NJ, Williams DR. Psychophysical estimate of extrafoveal cone spacing. J Opt Soc Am A 1987;4(8):1503–1513. [PubMed: 3625330]

41. Taylor, BN.; Kuyatt, CE. NIo-SaT. Guidelines for Evaluating and Expressing the Uncertainty of NIST Measurement Results. Washington, DC: U.S. Department of Commerce, Technology Administration; 1994. p. vNIST Technical Note 1297

42. Burns SA, He JC, Delori F. Do the cones see light scattered from the deep retinal layers. Vision Sci 1997;1:94–7.

43. Prieto PM, McLellan JS, Burns SA. Investigating the light absorption in a single pass through the photoreceptor layer by means of the lipofuscin fluorescence. Vision Res 2005;45(15):1957–1965. [PubMed: 15820514]

44. Curcio CA, Sloan KR. Packing geometry of human cone photoreceptors: variation with eccentricity and evidence for local anisotropy. Vis Neurosci 1992;9:169–180. [PubMed: 1504026]

45. Burke JM, Hjelmeland LM. Mosaicism of the retinal pigment epithelium: seeing the small picture. Mol Interv 2005;5(4):241–249. [PubMed: 16123538]

46. Bindewald-Wittich A, Han M, Schmitz-Valckenberg S, et al. Two-photon-excited fluorescence imaging of human PRE cells with a femtosceond Ti: Sapphire laser. Invest Ophthalmol Vis Sci 2006;47:4553–4557. [PubMed: 17003452]

47. Snodderly DM, Sandstrom MM, Leung IY-F, et al. Retinal pigment epithelial cell distribution in central retina of rhesus monkeys. Invest Ophthalmol Vis Sci 2002;43:2815–2818. [PubMed: 12202496]

48. Morgan JIW, Hunter JJ, Masella B, et al. Light-induced retinal changes observed using high-resolution autofluorescence imaging of the retinal pigment epithelium. Invest Ophthalmol Vis Sci 2008;49:3715–3729. [PubMed: 18408191]
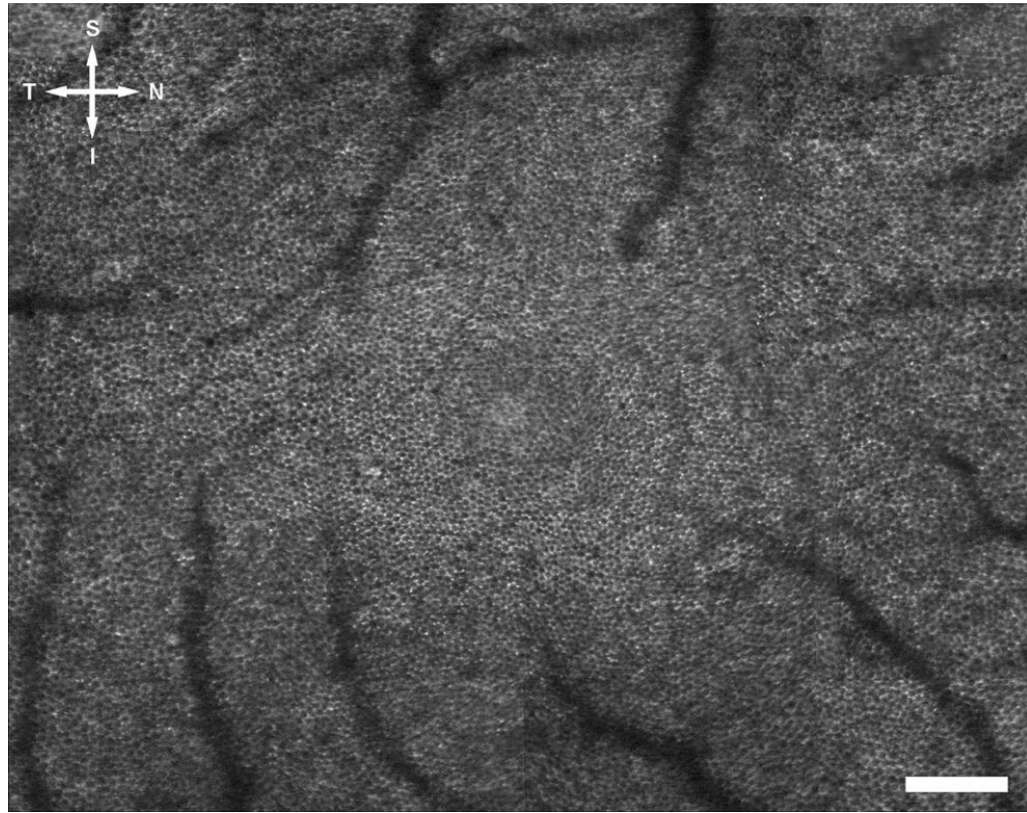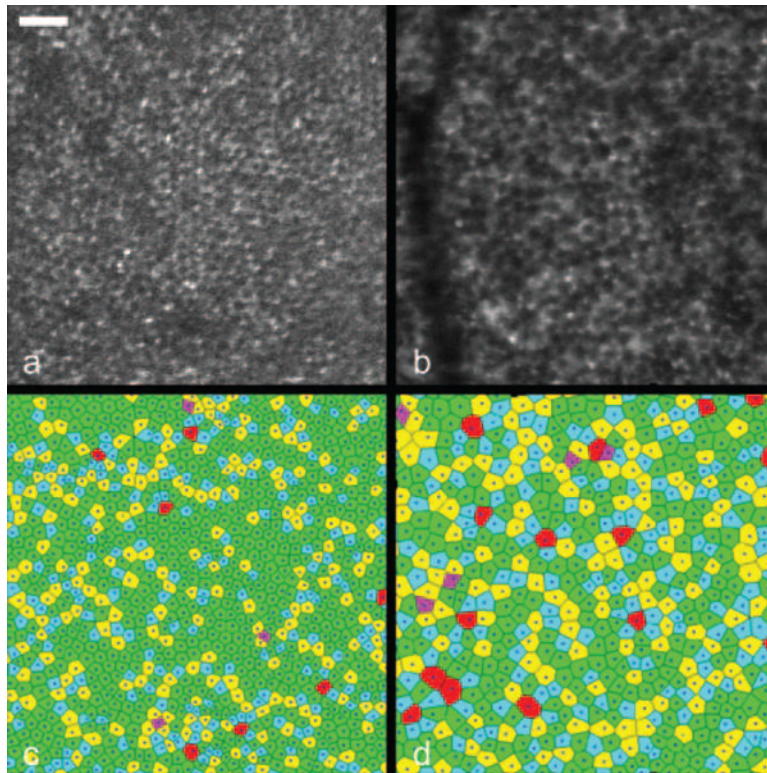
Figure 1.
The complete RPE mosaic in the right eye of monkey 320 as imaged in vivo with the AOSLO with autofluorescence imaging capabilities. Every RPE cell in the central fovea and surrounding area is clearly resolved in this image. S, superior; T, temporal; I, inferior; N, nasal. Scale bar, 200 μm.
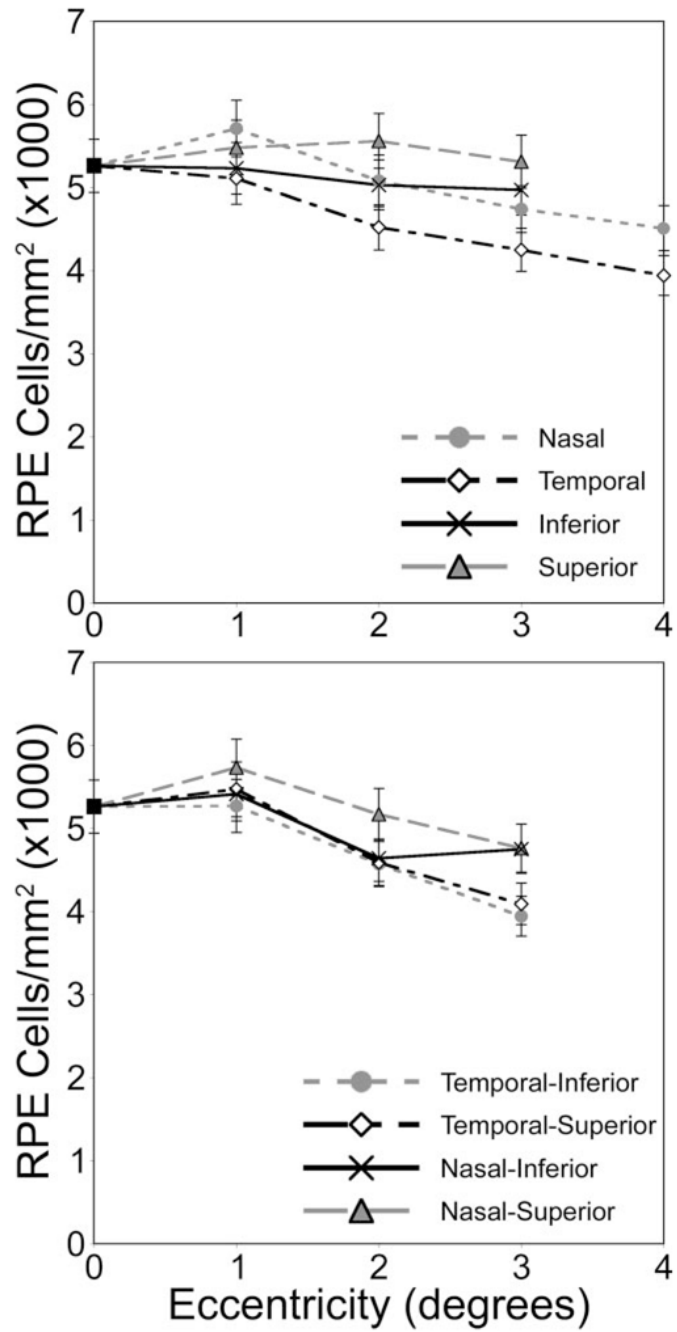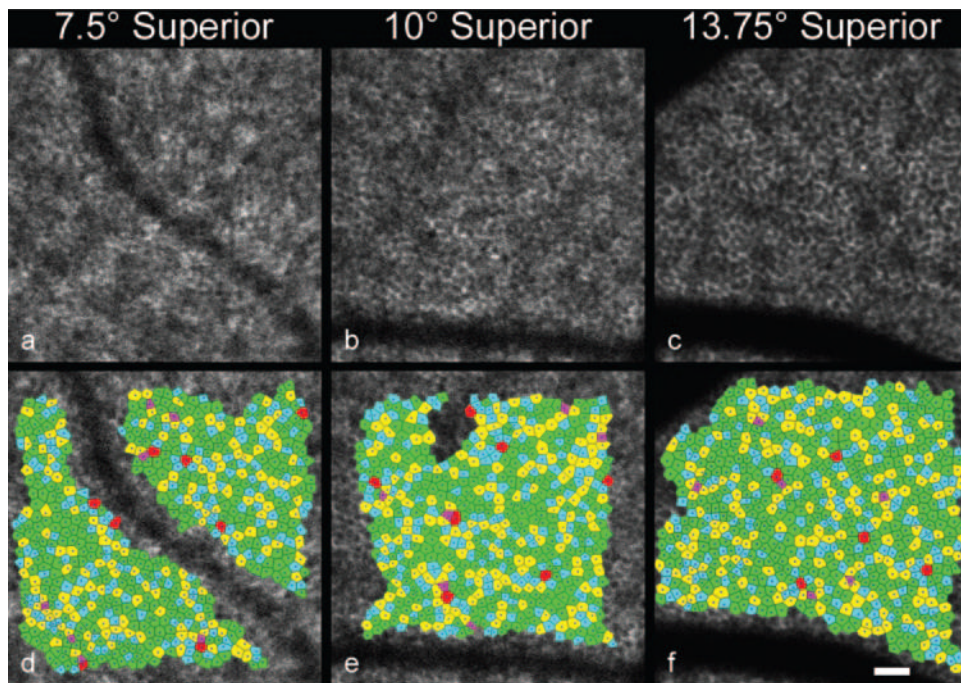
Figure 2.
RPE cell density as a function of eccentricity from the fovea, as measured from Figure 1. In this eye, peak RPE cell density is displaced from the fovea.
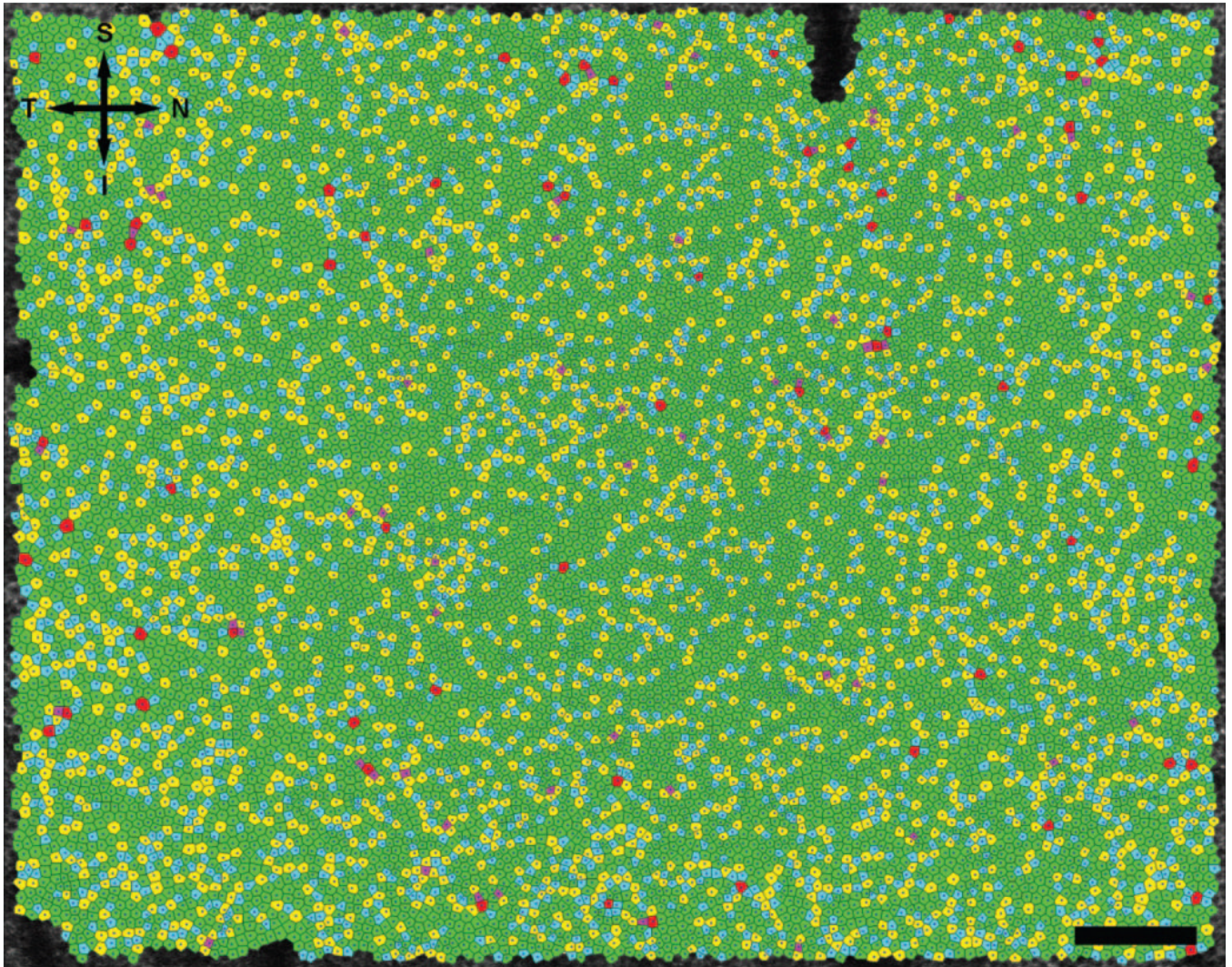
Figure 3.
Voronoi cell domain of the RPE cell mosaic shown in Figure 1 from the right eye of monkey 320. *Purple*, *blue*, *green*, *yellow*, and *red* cells have 4, 5, 6, 7, and 8 Voronoi neighbors, respectively. Directional labels are as in Figure 1. Scale bar, 200 μm.
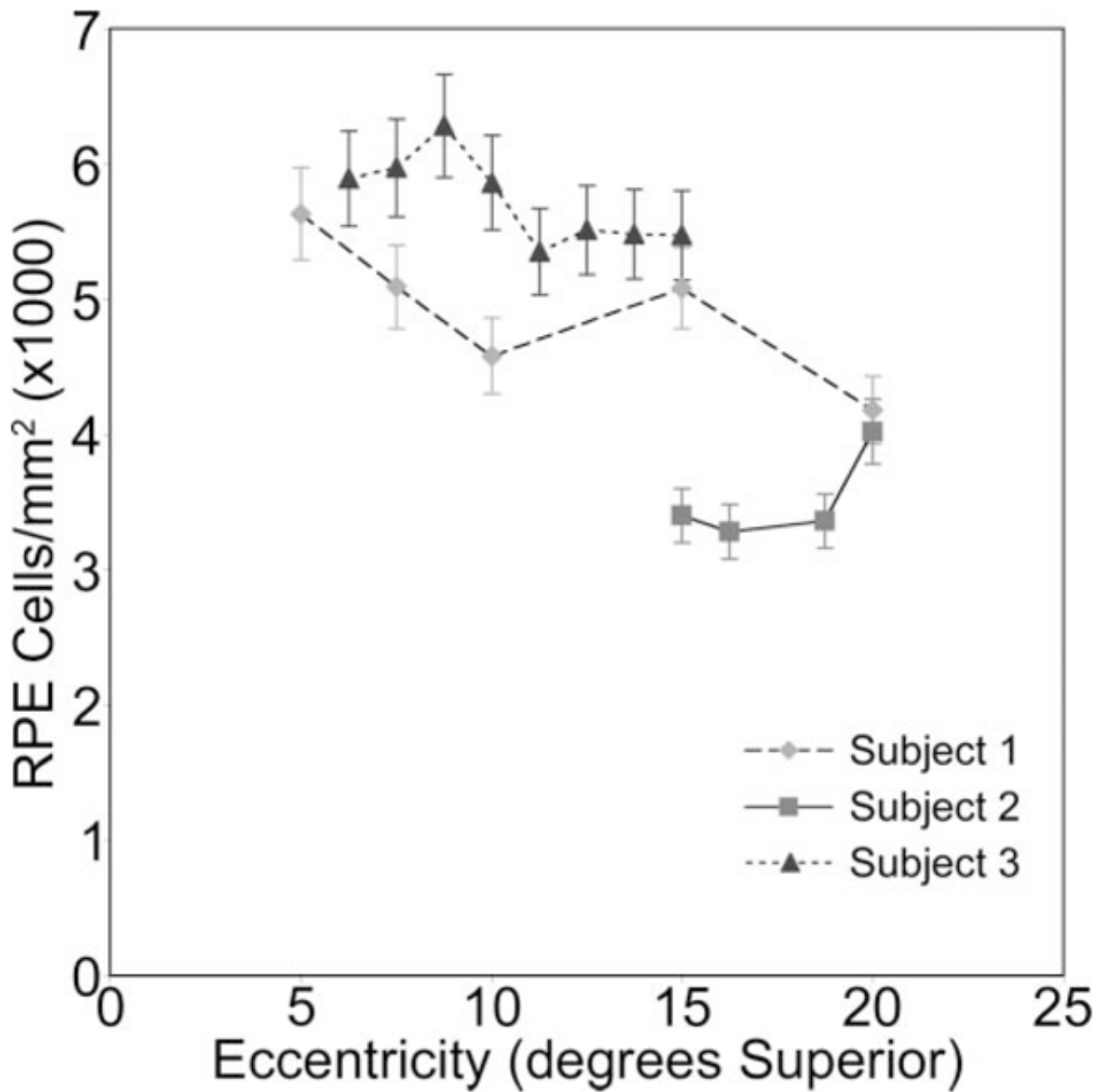
Figure 4.
RPE cell mosaics and corresponding Voronoi mosaics at 2° nasal (**a**, **c**) and approximately 6.5° temporal, 1° inferior (**b**, **d**) from the fovea in monkey 903. Cell density decreased as eccentricity increased and the RPE mosaic became less regular as eccentricity increased. Scale bar, 50 μm.

Figure 5.
RPE cell mosaics (**a**–**c**) and corresponding Voronoi domain mosaics (**d**–**f**) at three eccentricities (7.5° superior, 10° superior, and 13.75° superior, respectively) in subject 3. Scale bar, 50 μm.

Figure 6.
RPE cell density verses eccentricity in degrees superior from fixation for three normal human subjects. Overall, RPE cell density decreased with increasing eccentricity from fixation. Cell density varied between subjects.
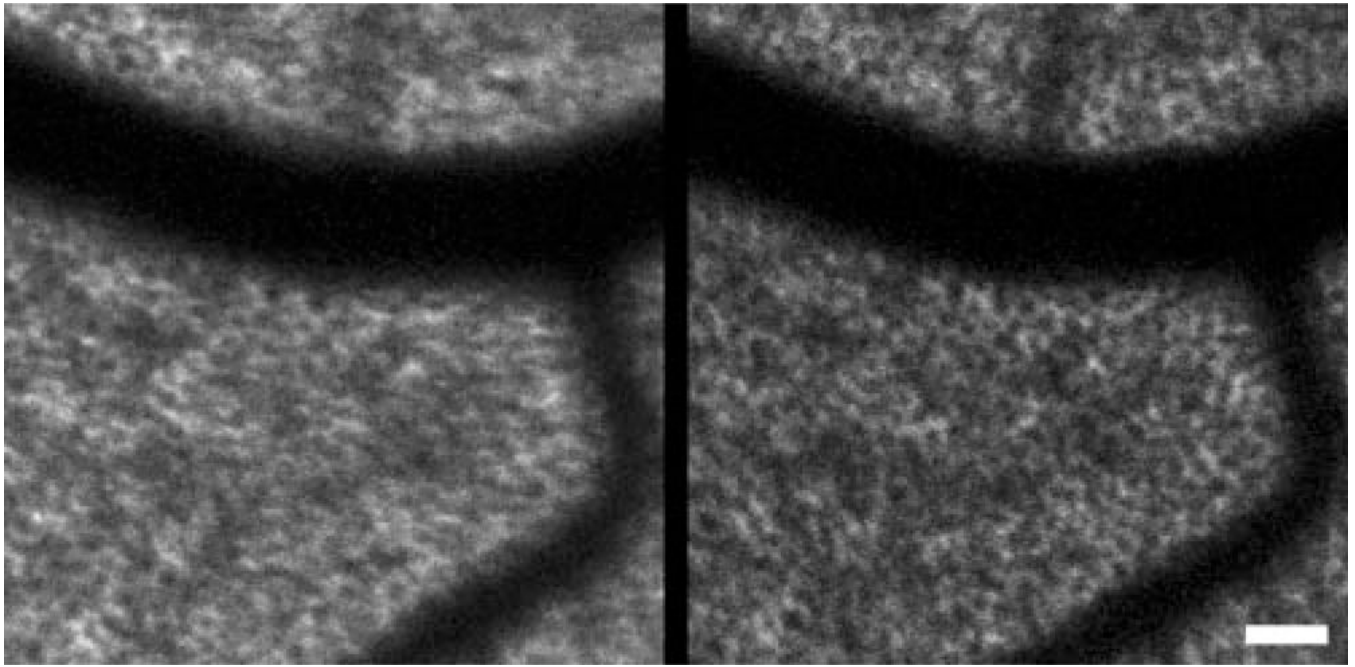
Figure 7.
RPE mosaic from subject 1 at 15° superior to fixation. The two images were taken 42 days apart. Each RPE cell identified in the first image can also be observed in the second image at the same position. Scale bar, 50 μm.
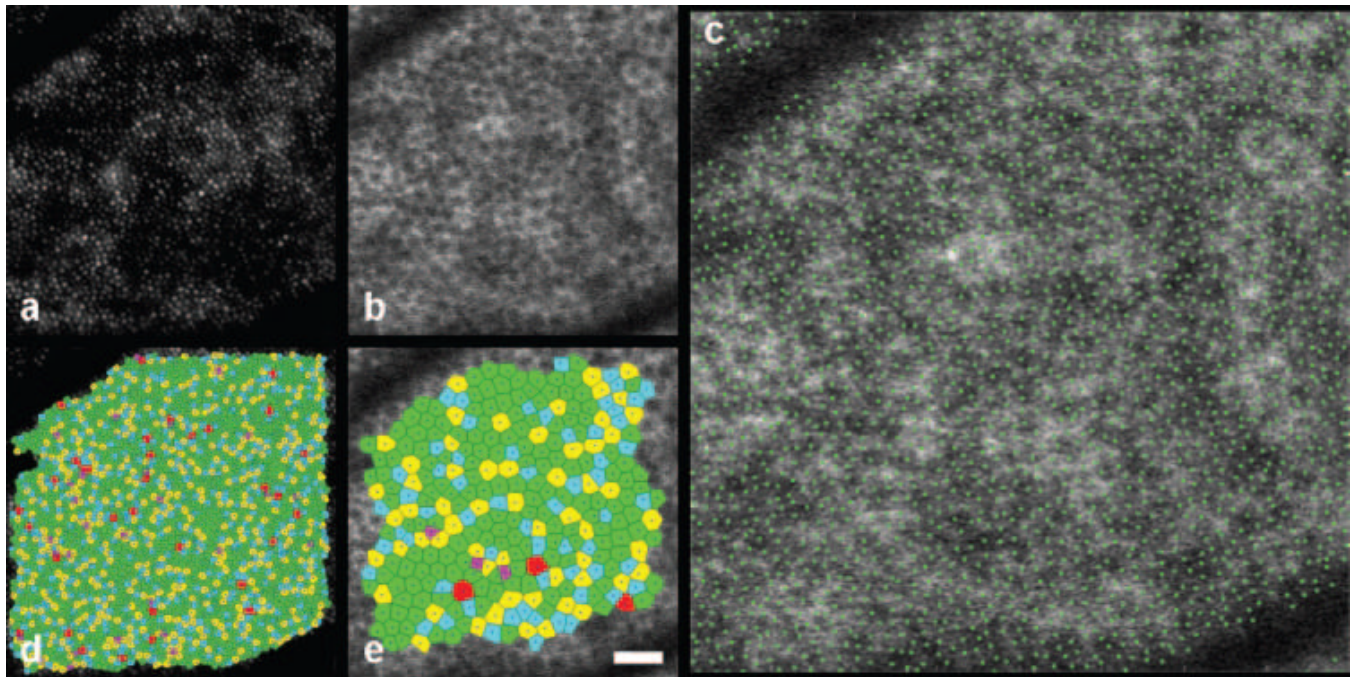
Figure 8.
Cone mosaic (**a**) and RPE mosaic (**b**) at approximately 4.5° nasal, 4.5° inferior in the left eye of monkey 320. The locations of the cone centers are plotted in *green* on top of the RPE cell mosaic (**c**). Voronoi domains are given for the cones (**d**) and the RPE cells (**e**). Scale bar, 50 μm.
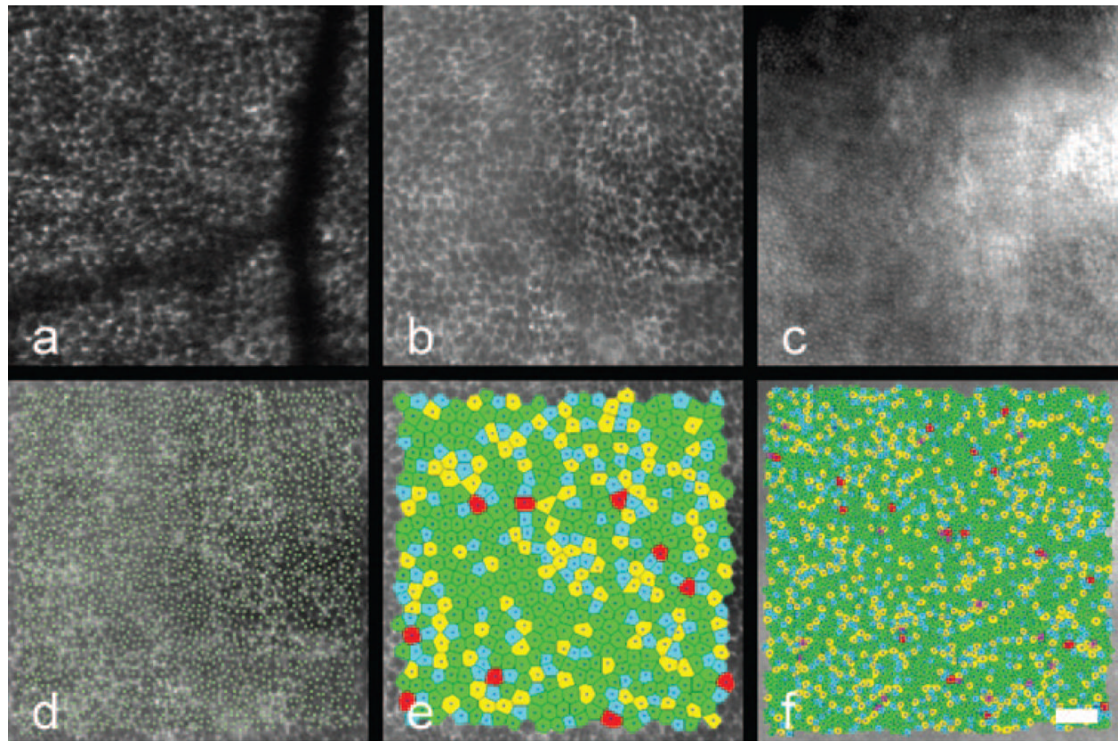
Figure 9.
RPE mosaic at approximately 6° temporal, 4.5° superior in the left eye of monkey 903 as imaged (**a**) in vivo with the AOSLO autofluorescence technique or (**b**) ex vivo using autofluorescence with a confocal microscope. (**c**) The cones at the same retinal location as (**b**) imaged using autofluorescence with the confocal microscope ex vivo. (**d**) The locations of cone centers (*green dots*) displayed on the corresponding RPE mosaic. Voronoi domain mosaics at the same location are illustrated for the RPE (**e**) and cone (**f**) mosaics from the confocal microscope ex vivo images. Scale bar, 50 μm.

Table 1

Statistics of the Spatial Arrangement of the RPE Cells in Monkey 320

Location (°) *	RPE Cell Density (Cells/mm²)†	Voronoi Area (μm²)†‡	Voronoi Sides (n)†‡	Observed NND (μm)†‡	Triangularly Packed NND (μm)§	Ratio//
Fovea	5,260 ± 320	190 ± 30	6.00 ± 0.61	11.6 ± 1.5	14.8	0.783
1 T	5,110 ± 310	196 ± 33	6.01 ± 0.57	12.1 ± 1.8	15.0	0.803
2 T	4,520 ± 270	221 ± 41	5.99 ± 0.61	12.9 ± 1.9	16.0	0.810
3 T	4,250 ± 260	235 ± 39	6.01 ± 0.67	13.3 ± 1.7	16.5	0.806
4 T	3,940 ± 240	254 ± 45	5.99 ± 0.64	13.7 ± 1.9	17.1	0.799
1 N	5,710 ± 340	175 ± 31	6.00 ± 0.53	11.5 ± 1.5	14.2	0.807
2 N	5,080 ± 310	197 ± 32	6.01 ± 0.56	12.2 ± 1.5	15.1	0.809
3 N	4,740 ± 280	208 ± 35	6.00 ± 0.62	12.3 ± 1.8	15.6	0.791
4 N	4,510 ± 270	222 ± 38	5.99 ± 0.68	13.1 ± 1.6	16.0	0.818
1 S	5,480 ± 330	182 ± 30	6.02 ± 0.63	11.3 ± 1.7	14.5	0.781
2 S	5,560 ± 330	180 ± 32	5.98 ± 0.61	11.6 ± 1.7	14.4	0.808
3 S	5,310 ± 320	188 ± 30	5.99 ± 0.61	11.9 ± 1.4	14.7	0.809
1 I	5,230 ± 310	191 ± 32	6.03 ± 0.63	11.8 ± 1.4	14.9	0.792
2 I	5,030 ± 300	199 ± 37	5.96 ± 0.63	11.9 ± 1.4	15.2	0.783
3 I	4,970 ± 300	201 ± 33	6.00 ± 0.70	12.2 ± 1.8	15.2	0.798
1 T, 1 S	5,470 ± 330	183 ± 30	6.00 ± 0.55	11.5 ± 1.5	14.5	0.793
2 T, 2 S	4,590 ± 280	218 ± 40	6.01 ± 0.65	12.8 ± 1.8	15.9	0.807
3 T, 3 S	4,090 ± 250	245 ± 43	6.00 ± 0.64	13.5 ± 1.8	16.8	0.803
1 T, 1 I	5,270 ± 320	190 ± 30	6.02 ± 0.60	11.9 ± 1.6	14.8	0.801
2 T, 2 I	4,570 ± 270	219 ± 38	6.00 ± 0.68	12.7 ± 1.7	15.9	0.799
3 T, 3 I	3,940 ± 240	254 ± 45	6.01 ± 0.67	13.6 ± 2.0	17.1	0.792
1 N, 1 S	5,730 ± 340	175 ± 27	5.97 ± 0.63	11.8 ± 1.6	14.2	0.829
2 N, 2 S	5,170 ± 310	193 ± 36	5.97 ± 0.63	11.8 ± 1.6	14.9	0.790
3 N, 3 S	4,760 ± 290	210 ± 37	5.97 ± 0.65	12.2 ± 1.9	15.6	0.781
1 N, 1 I	5,410 ± 320	185 ± 32	5.97 ± 0.57	11.2 ± 1.6	14.6	0.770
2 N, 2 I	4,640 ± 280	215 ± 40	6.00 ± 0.58	12.2 ± 1.5	15.8	0.776
3 N, 3 I	4,750 ± 290	211 ± 41	5.96 ± 0.63	12.8 ± 1.8	15.6	0.822

*
Location of the center of the region as measured in degrees from the fovea in the direction of T, temporal; N, nasal; S, superior; I, inferior.

†
The uncertainty in cell density is assumed to be 6%.[37]

‡
Mean ± SD.

§
Calculated NND as expected for a perfectly triangularly packed mosaic with a density equal to that observed for each location.

//
Ratio of observed mean NND to the triangularly packed mosaic NND. Lower ratios indicate a larger departure from a perfectly packed mosaic.

Statistics of the Spatial Arrangement of the RPE Cell Mosaic

Table 2

Location (°)*	RPE Cell Density (Cells/mm²)†	Voronoi Area (μm²)†‡	Voronoi Sides (n)†‡	Observed NND (μm)†‡	Triangularly Packed NND (μm)§	Ratio//
Subject 1						
5 S	5,630 ± 340	178 ± 48	5.99 ± 0.75	10.8 ± 1.7	14.3	0.755
7.5 S	5,090 ± 310	195 ± 37	5.96 ± 0.71	11.7 ± 1.6	15.1	0.775
10 S	4,580 ± 280	218 ± 52	5.96 ± 0.73	12.1 ± 2.1	15.9	0.761
15 S	5,080 ± 300	197 ± 36	5.98 ± 0.72	11.8 ± 1.7	15.1	0.781
20 S	4,180 ± 250	239 ± 55	6.02 ± 0.81	12.6 ± 2.1	16.6	0.759
Subject 2						
15 S	3,400 ± 200	294 ± 60	6.00 ± 0.72	14.1 ± 2.2	18.4	0.766
16.25 S	3,280 ± 200	305 ± 59	5.98 ± 0.72	14.3 ± 2.1	18.8	0.761
18.75 S	3,360 ± 200	297 ± 65	5.98 ± 0.79	14.2 ± 2.2	18.5	0.768
20 S	4,020 ± 240	249 ± 48	5.98 ± 0.74	12.9 ± 1.9	17.0	0.759
Subject 3						
6.25 S	5,890 ± 350	170 ± 30	5.98 ± 0.75	10.8 ± 1.6	14.0	0.771
7.5 S	5,970 ± 360	168 ± 33	5.98 ± 0.74	10.5 ± 1.7	13.9	0.755
8.75 S	6,280 ± 380	159 ± 34	5.99 ± 0.78	10.3 ± 1.9	13.6	0.757
10 S	5,860 ± 350	171 ± 34	5.98 ± 0.78	10.7 ± 1.8	14.0	0.764
11.25 S	5,350 ± 320	187 ± 35	5.99 ± 0.69	11.3 ± 1.8	14.7	0.769
12.5 S	5,510 ± 330	182 ± 41	5.79 ± 0.70	11.1 ± 1.9	14.5	0.766
13.75 S	5,480 ± 330	182 ± 36	5.99 ± 0.73	11.2 ± 1.7	14.5	0.772
15 S	5,470 ± 330	183 ± 36	5.97 ± 0.75	11.1 ± 1.8	14.5	0.766
Animal 903						
2 N	6,730 ± 400	149 ± 28	6.00 ± 0.66	10.3 ± 1.6	13.1	0.786
6.5 T, 1 I	3,620 ± 220	276 ± 58	6.00 ± 0.80	13.7 ± 2.0	17.9	0.765

*
Location of the center of the region as measured in degrees from the fovea in the direction of T, N, S, I. Abbreviations as in Table 1.

†
The uncertainty in cell density is assumed to be 6%.[37]

‡
Mean ± SD.

§
Calculated NND as expected for a perfectly triangularly packed mosaic with a density equal to that observed for each location.

//
Ratio of observed mean NND to the triangularly packed mosaic NND. Lower ratios indicate a larger departure from a perfectly packed mosaic.

Table 3

Statistics of the Spatial Arrangement of the Cone and RPE Cell Mosaic

Cell Type and Location (°)[*]	RPE Cell Density (Cells/mm²)[†]	Voronoi Area (μm²)[‡]	Voronoi Sides (n)[‡]	Observed NND (μm)[‡]	Triangularly Packed NND (μm)[§]	Ratio[‖]
Animal 320; 4.5° N, 4.5° I; in vivo						
Cones	22,700 ± 1,400	44 ± 7	5.99 ± 0.75	5.5 ± 0.9	7.1	0.775
RPE	4,180 ± 250	239 ± 40	5.99 ± 0.70	13.1 ± 1.9	16.6	0.789
Animal 903; 6° T, 4.5° S; in vitro						
Cones	15,150 ± 910	66 ± 12	5.96 ± 0.70	6.8 ± 1.0	8.7	0.782
RPE	3,710 ± 220	270 ± 42	5.99 ± 0.70	14.2 ± 1.8	17.6	0.807

[*] Location of the center of the region as measured in degrees from the fovea in the direction of T, N, S, I. Abbreviations as in Table 1.

[†] The uncertainty in cell density is assumed to be 6%.[37]

[‡] Mean ± SD.

[§] Calculated NND as expected for a perfectly triangularly packed mosaic with a density equal to that observed for each location.

[‖] Ratio of observed mean NND to the triangularly packed mosaic NND. Lower ratios indicate a larger departure from a perfectly packed mosaic.